Supporting Information for

High-Performance Ammonia Oxidation Catalysts for Anion Exchange Membrane Direct Ammonia Fuel Cells

Yi Li[a,b,1], Hemanth Somarajan Pillai[c,1], Teng Wang[d, 1], Sooyeon Hwang [e,1], Yun Zhao[d], Zhi Qiao[a], Qingmin Mu[c], Stavros Karakalos[f], Mengjie Chen[a], Juan Yang*[b], Dong Su[e], Hongliang Xin*[c], Yushan Yan*[d], Gang Wu*[a]

[a] Department of Chemical and Biological Engineering, University at Buffalo, The State University of New York, Buffalo, NY 14260, USA.

[b] School of Materials Science and Engineering, Jiangsu University, Zhenjiang, 212013, China.

[c] Department of Chemical Engineering, Virginia Polytechnic Institute and State University, Blacksburg, Virginia 24061, USA.

[d] Department of Chemical and Biomolecular Engineering, Center for Catalytic Science and Technology, University of Delaware, Newark, DE 19716, USA.

[e] Center for Functional Nanomaterials, Brookhaven National Laboratory, Upton, New York 11973, USA.

[f] Department of Chemical Engineering, University of South Carolina, Columbia, South Carolina 29208, USA.

*Corresponding authors: yangjuan6347@ujs.edu.cn (J. Yang); hxin@vt.edu (H. Xin);

yanys@udel.edu (Y. Yan); and gangwu@buffalo.edu (G. Wu)

[1]These authors contributed equally.

Experimental Details
Computational Details
Fuel Cell Testing Details
Figures S1 to S21
Table S1 to S6
References

Experimental Details

1. *Catalyst Synthesis*

1.1 Synthesis of zeolitic imidazolate framework-8 (ZIF-8) derived carbon and pretreatment of CeO$_2$

ZIF-8 was prepared using a solution method according to our previous report[1]. Typically, 6.777 g of zin (Ⅱ) nitrate hexahydrate were dissolved in 100 mL of methanol in a round-bottom flask. The other 100 mL of methanol solution contained 7.874 g of 2-methylimidazole. Then these two solutions were mixed and heated at 60ºC for 24 h for ZIF-8 nanocrystal synthesis. Subsequently, the ZIF-8 nanocrystals were washed at least three times with ethanol via centrifugation and then dried at 50ºC in a vacuum oven overnight. The ZIF-8 precursors were heated at 950ºC in a tube furnace under Ar flow for 3 h to obtain the final ZIF-8 carbon. The commercial CeO$_2$ was purchased from Alfa Aesar Company, which was dispersed in 0.01 M NaOH and ultrasonicated for 1.0 h. Then the CeO$_2$ was collected by centrifugation, washed with deionized (DI) water, and dried at 50ºC in a vacuum oven overnight.

1.2 Method to deposit PtIrZn nanoparticles on ZIF-8 carbon and CeO$_2$ composite support.

Pt-based nanoparticle deposition onto the ZIF-8 carbon and CeO$_2$ composite support was performed through a sodium borohydride reduction method with a controlled precious-group-metal (PGM, Pt or PtIr, molar ratio of Pt:Ir = 1:1) loading of 10 wt%. In a typical procedure, the pretreated CeO$_2$ and ZIF-8 derived carbon with a total amount of 120 mg and mass ratio of 2:1 were added into a mixed solution (80 mL) containing ethanol and DI water with a volume ratio of 1:1, and then the mixture was ultrasonicated for 1.0 h to prepare a homogeneous dispersion. Subsequently, potassium chloroplatinate (0.1 M), chloro-iridic acid (0.1 M), and zin (Ⅱ) nitrate hexahydrate (0.1 M) aqueous solutions were added into the dispersion ultrasonication for 2.0 h,

and then magnetically stirred for another 2.0 h. After that, the dispersion was placed in ultrasonic environment, and 10 mL of sodium borohydride (1.0 g) aqueous solution was dropped wisely into the dispersion. During the reaction process, obvious bubbles can be seen from the solution due to a strong reaction between the reducing agent and the metal ions. To make sure the reaction was completed, the mixture should be ultrasonicated for at least 3.0 h. The products were collected after washing with DI water several times until no Cl^- could be detected by $AgNO_3$ solution and drying at 50ºC in a vacuum oven overnight. The as-prepared catalysts were designed as $PtIrZn_x/CeO_2$-ZIF-8 (x=1, 2, or 3). Molar ratios of Pt:Ir:Zn in the $PtIrZn_x/CeO_2$-ZIF-8 (x=1, 2 or 3) catalysts were confined to 1:1:0.2, 1:1:0.6, and 1:1:1, correspondingly. Other samples (e.g., Pt/CeO_2-ZIF-8, $PtIr/CeO_2$-ZIF-8, and $PtZn/CeO_2$-ZIF-8 in molar ratio of Pt:Ir and Pt:Zn = 1:1, as well as $PtIrNi_2/CeO_2$-ZIF-8 and $PtIrCu_2/CeO_2$-ZIF-8 in molar ratio of Pt:Ir:Ni and Pt:Ir:Cu = 1:1:0.6) were prepared using a similar procedure and the corresponding metal precursors.

2. Physical Characterization

Catalyst morphology was conducted on a Hitachi SU 70 scanning electron microscopy (SEM) at a working voltage of 5 kV. The N_2 isothermal adsorption/desorption was studied on a Micromeritics TriStar II, and the samples were degassed at 150ºC for 5 h under vacuum before the tests. The microstructure characterization of the catalyst was performed on JEOL JEM-2100F at an accelerating voltage of 200 kV to obtain bright field and high-resolution transmission electron microscopy (HRTEM) images. The high angle annular dark-field (HAADF) scanning transmission electron microscopy (STEM) images and elemental mappings were conducted on a high-resolution analytical scanning/transmission electron microscope (STEM, FEI Talos F200X, operating at 200 keV) equipped with a four-quadrant 0.9-sr energy-dispersive X-ray spectrometer (EDS). The crystalline phases of the catalysts were carried out on powder X-ray diffraction (XRD) on a Rigaku

Ultima IV diffractometer with Cu Kα X-rays. X-ray photoelectron spectroscopy (XPS) was conducted on a Kratos AXIS Ultra DLD XPS system equipped with a hemispherical energy analyzer and a monochromatic Al K_α source.

3. Electrochemical Measurements

Electrochemical measurements were performed on an electrochemical workstation (CHI760b) coupled with a rotating disk electrode (RDE, PINE, AFMSRCE 3005) in a three-electrode cell. A graphite rod and an Hg/HgO (filled with 1.0 M KOH) electrode were used as the counter and reference electrodes, respectively. At high testing temperatures (25–80 ºC), we used a reference electrode of Ag/AgCl (KCl-sat.) which was bought from Metrohm. All the reference electrodes were calibrated to a reversible hydrogen electrode (RHE) in the same electrolyte solution before each test. A rotating ring-disk electrode (RRDE, diameter: 5.6 mm) and an RDE (diameter: 5.0 mm) electrode covered by a thin film of the catalyst were used as the working electrodes at room and high temperatures (25-80ºC), respectively. For AOR activity comparison, the commercial PtIr/C catalysts (Premetek, 40 wt%, Pt:Ir molar ratio 1:1) were measured at similar testing conditions. For working electrode preparation, 2 mg catalyst was ultrasonically dispersed in a 1.0 mL mixture containing isopropanol and Nafion (6 μL, 5 wt.%) solution to form a catalyst ink. Then, the catalyst ink was drop-casted onto the disk electrode with a specific loading of 20 μg_{PGM} cm^{-2} and dried at room temperature to yield a thin-film electrode. For the electrolyte in absence of NH_3, the catalyst-coated disk working electrode was first subjected to cyclic voltammetry (CV) in Ar-saturated 1.0 M KOH at a scan rate of 50 mV s^{-1} to activate the catalysts and then recorded at a scan rate of 20 mV s^{-1} with an RDE rotating speed of 900 rpm. For the electrolyte in presence of NH_3, the AOR activity of the catalyst was characterized by CV measurements in 1.0 M KOH + 0.1 M NH_3 solution at a scan rate of 5 mV s^{-1} with a similar RDE rotating speed. AOR stability

tests were recorded in 1.0 M KOH + 0.1 M NH_3 electrolyte before and after 2000 potential cycles. The CV cycles were recorded in the potential range of 0.05–0.7 V in Ar-saturated 1.0 M KOH at a scanning rate of 500 mV s^{-1}. The NH_3 loaded electrolyte solution was prepared by mixing NH_3 solution (28.0–30.0%, ACS-Reagenz) with KOH and DI water. In the NH_3 oxidation tests, a reduction potential (–0.8 V *vs.* SHE) holding for 100 s was employed to recover the catalyst when the catalyst was used in subsequent tests (generally, the CVs and i-t curves for the same electrode). For the experiments of operating temperature, NH_3 concentration, and KOH concentration effects, a fresh electrode was used for every single test and a similar electrochemical cleaning procedure was followed as an aforementioned method. Electrochemical impedance spectroscopy (EIS) measurements were measured at the catalysts' corresponding open circuit potential in the frequency range of 10^{-2} to 10^6 Hz with 10 mV sinusoidal perturbations and 12 steps per decade in 1.0 M KOH solution. Furthermore, all the remained CV curves were used the same potential cycling protocols to describe the different AOR catalysts.

Computational Details

DFT Calculations

Non-spin polarized DFT calculations were performed using Vienna Ab Initio Simulation Package (VASP) with projector augmented pseudopotentials. A plane wave energy cutoff of 450 eV was used and the exchange-correlation was approximated at the GGA level using RPBE. A vacuum of 15 Å was used on both sides of the slab such that there was 30 Å between mirror images. All slabs had 4 layers where the bottom two were fixed during geometry optimization. Geometries were considered optimized when the maximum force was less than .05 eV/Å. All slabs were simulated using a 4 x 2 supercell and a 3 x 6 x 1 Monkhorst-Pack mesh was used to sample the Brillouin zone. Methfessel-Paxton smearing was used with a smearing parameter of 0.1 eV and energies

were extrapolated to $k_BT = 0$ eV. DFT energies for molecules were calculated via a Gamma point calculation of the molecule in a 15 Å x 16 Å x 17 Å box. Bulk lattice constants were optimized via geometry optimizations using a 12 x 12 x 12 k-point. Solvation was included through the use of VASPsol. For solvation, the dielectric constant was set to 78.4 while the Debye screening length was set to 3 Å. Precision was set to "Accurate" and the surface tension parameter was set to 0.

To create the different surfaces first the bulk Pt_2Ir_2 was optimized to a lattice constant of 3.94 Å. Using this bulk, a surface with the (100) termination was created as the model system. To simulate the various Zn concentrations, different surface/subsurface atoms were replaced with Zn atoms. DFT energies were converted into free energies by adding the appropriate corrections from our previous calculations.

Fuel Cell Testing Details

PAP polymers based on terphenyl group were employed as HEMs and ionomer. The ink for spraying the electrode was prepared by adding catalyst and ionomer to isopropanol solvent, followed by sonication for 1 h. The weight ratio of catalyst and ionomer was 9:1 for anode and 4:1 for cathode respectively. Then two types of ink for anode and cathode were sprayed onto hydrophilic carbon cloth (ELAT) and HEM respectively by airbrush to produce 5 cm^2 electrodes. The final catalyst loading was 1.0 mg_{PGM} cm^{-2} for the anode and 2 mg cm^{-2} for Acta 4020 catalyst. Then the MEA was assembled with two electrodes, fluorinated ethylene propylene (FEP) gasket, SGL 29 BC for cathode gas diffusion layer, a pair of graphite bipolar plates with 5 cm^2 flow field (ElectroChem), and gold-coated current collectors to complete the full ammonia fuel cell.

The polarization curves and power density curves were obtained by using a fuel cell test station (Scribner-Associates 890e). At the same time, the high-frequency resistance at 5 kHz of the cell was monitored continuously by an EIS module built into the fuel cell test system. An

aqueous solution of 7 M NH_3+ 1.25 M KOH was pumped to the anode flow field at 5 mL min^{-1}, while 500 mL min^{-1} O_2 gas flow passed through a humidifier at 95 ºC before it went through the cathode flow field. Specific backpressure was applied on each side of the cell by a gas regulator.
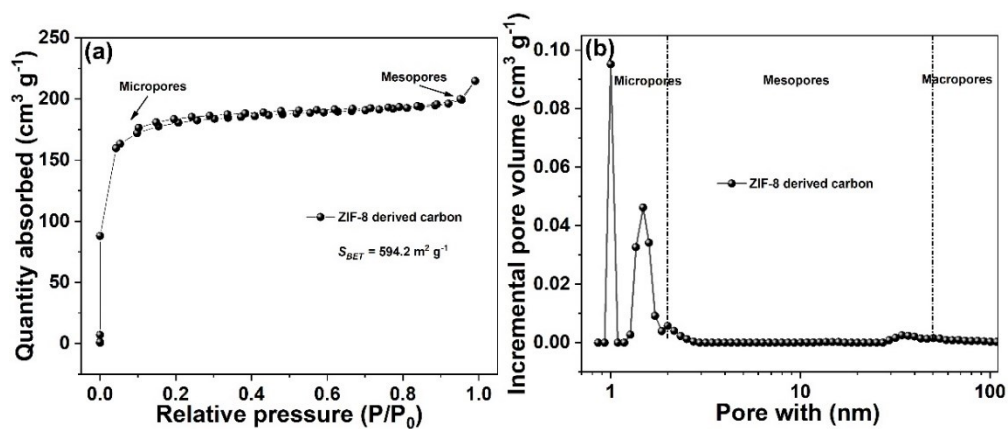
Figure S1. (a) N_2 adsorption/desorption isotherms and (b) pore size distributions of the porous ZIF-8 derived carbon. These results show a large surface area of 594.2 m^2g^{-1} and porous architecture for the ZIF-8 derived carbon.
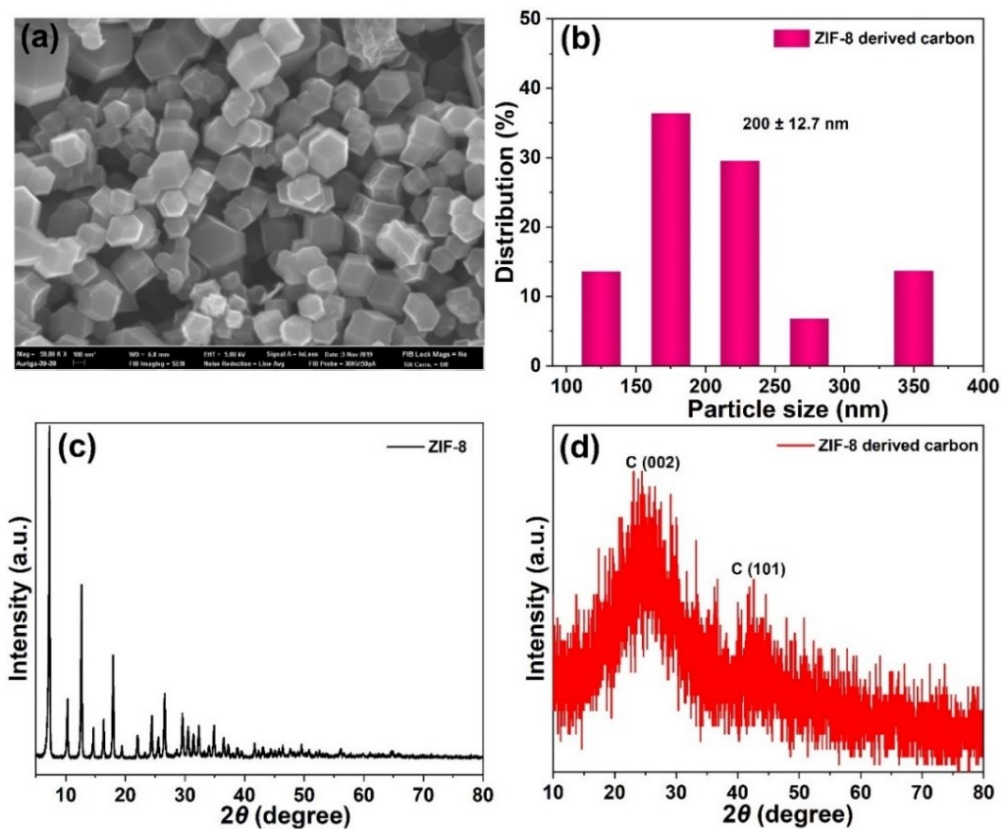
Figure S2. SEM image of ZIF-8 derived carbon (a), and the corresponding particle size distributions (b). (c, d) XRD patterns of ZIF-8 and ZIF-8 derived carbon, respectively. SEM image and particle size distributions of ZIF-8 derived carbon demonstrate that ZIF-8 with a particle size of 200 ± 12.7 nm shows a monodispersed rhombic dodecahedron structure. XRD pattern results suggest that crystal ZIF-8 precursors are converted to the carbon phase after a thermal annealing process (950ºC under Ar atmosphere).
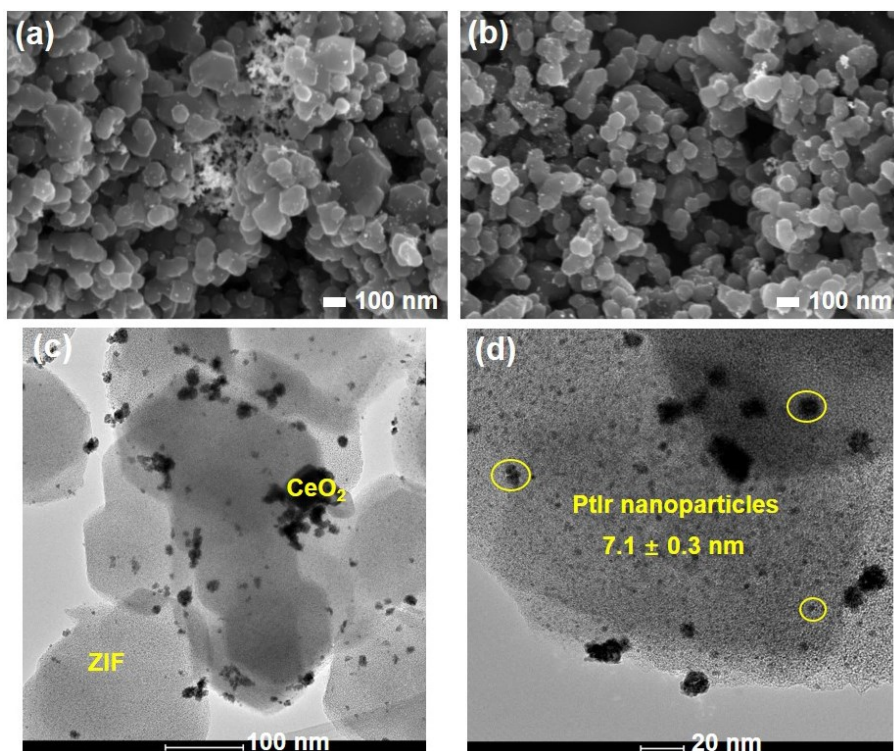
Figure S3. (a, b) SEM images of the PtIr/CeO$_2$-ZIF-8 product show that bimetallic PtIr nanoparticles are deposited on composite support of CeO$_2$ and ZIF-8 derived carbon. Except for some aggregated PtIr nanoparticles, most areas show a relatively uniform particle distribution. (c, d) TEM images of the PtIr/CeO$_2$-ZIF-8 product show that composite support of CeO$_2$ and ZIF-8 derived carbon is supported with bimetallic PtIr nanoparticles with an average particle size of 7.1 ± 0.3 nm, yet some aggregates are also observed.
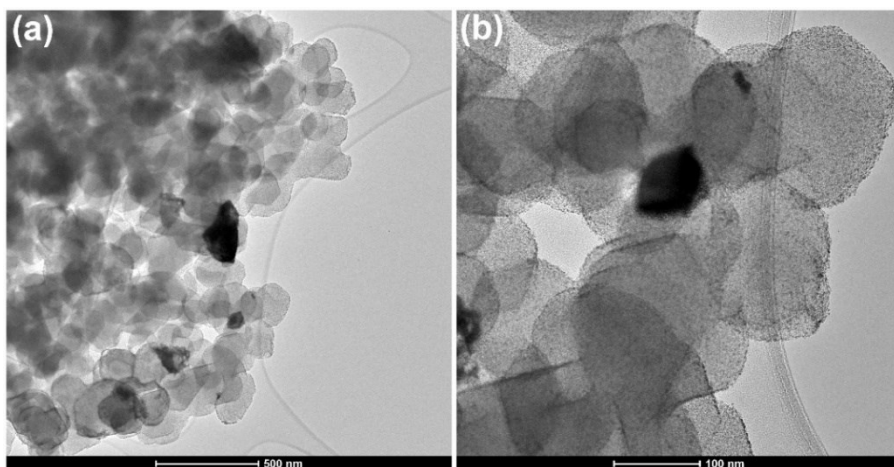
Figure S4. (a, b) TEM images of the PtIrZn$_2$/CeO$_2$-ZIF-8 product show that PtIrZn ternary nanoparticles with uniform size are well distributed on the composite support of CeO$_2$ and ZIF-8 derived carbon.
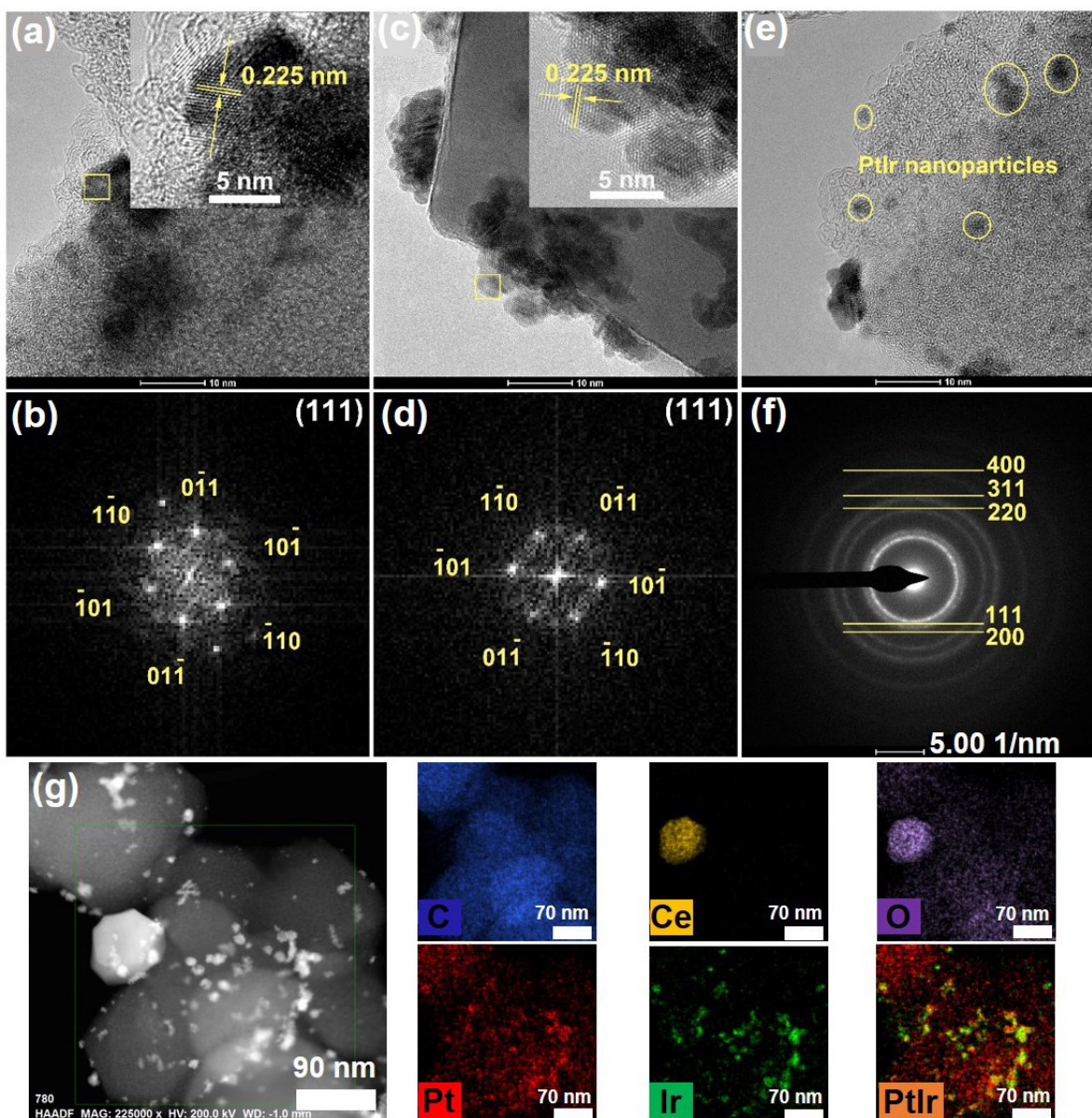
Figure S5. Morphology, structure, and composition of the PtIr/CeO$_2$-ZIF-8. (a, c, and e) HR-TEM images, (b, d) the corresponding Fast-Fourier-Transform (FFT) patterns from the selected area of ZIF-8 derived carbon (a) and CeO$_2$ (c) supports, and (f) is the electron diffraction (ED) pattern of a selected area. (g) HAAD-STEM images and its corresponding EDS elemental mappings of C, Ce, O, Pt, Ir, and integrated mapping of Pt and Ir demonstrate that the PtIr nanoparticles are distributed relatively uniform throughout the support, yet some aggregates are also observed in PtIr/CeO$_2$-ZIF-8.
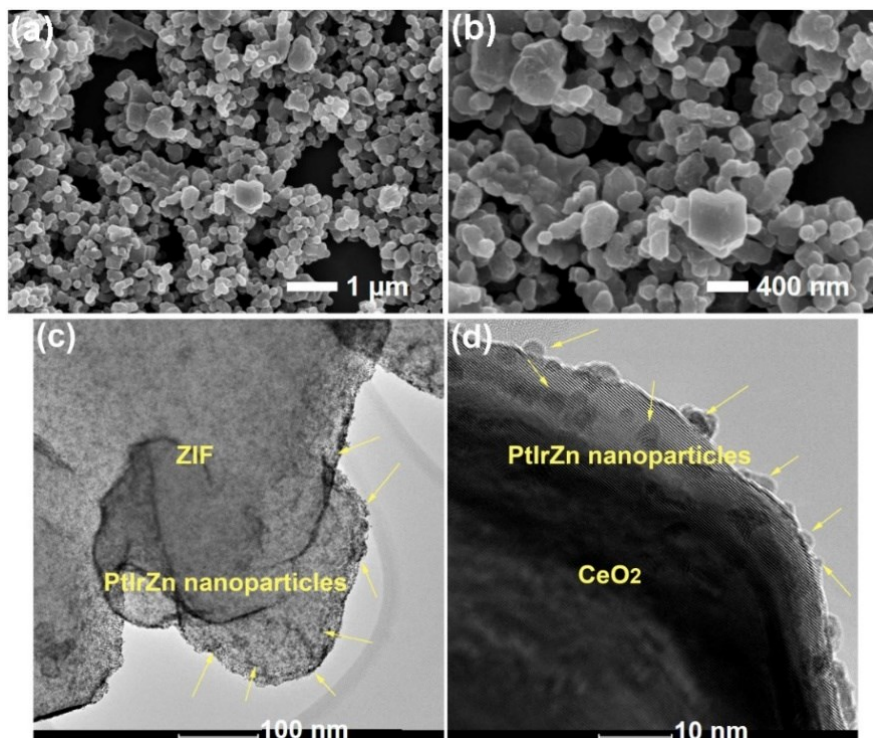
Figure S6. (a, b) SEM and (c, d) TEM images of the PtIrZn$_2$/CeO$_2$-ZIF-8 product show that trimetallic PtIrZn nanoparticles are uniformly deposited on composite support of CeO$_2$ and ZIF-8 derived carbon.
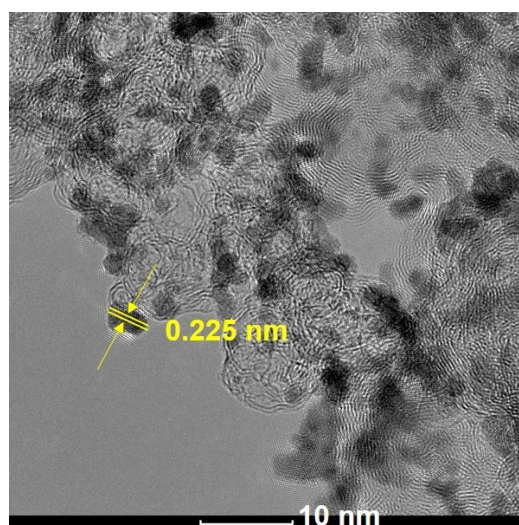
Figure S7. HR-TEM image of the commercial PtIr/C suggests that PtIr nanoparticles with a diameter of 2.7 ± 0.3 nm are uniformly distributed on the carbon black (XC-72). Additionally, the PtIr NPs show an interplanar spacing of 0.225 nm.
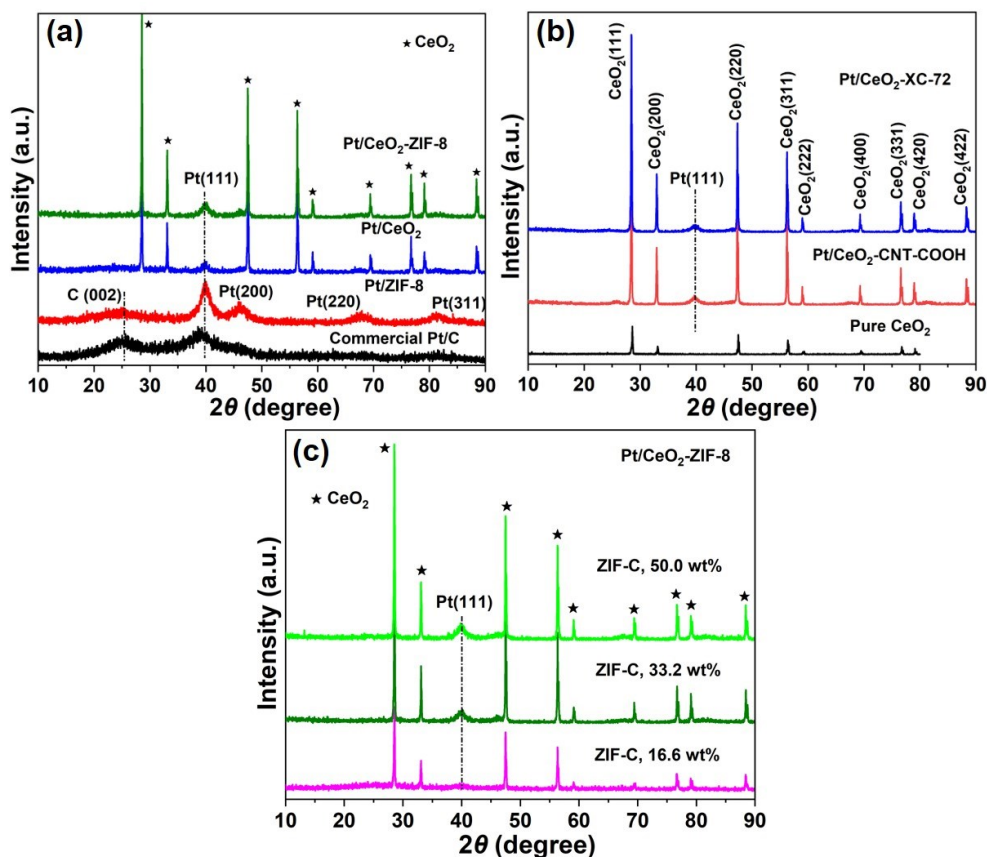
Figure S8. XRD patterns of the synthesized catalysts. (a) commercial Pt/C, Pt-ZIF-8, Pt-CeO$_2$, and Pt-CeO$_2$-ZIF-8, (b) Pure CeO$_2$, Pt/CeO$_2$-CNT-COOH, and Pt/CeO$_2$-XC-72, and (c) Pt/CeO$_2$-ZIF-8 with different carbon contents (16.6 wt%, 33.2 wt%, and 50.0 wt%). These XRD patterns indicate the successful deposition of Pt nanoparticles on different supports.
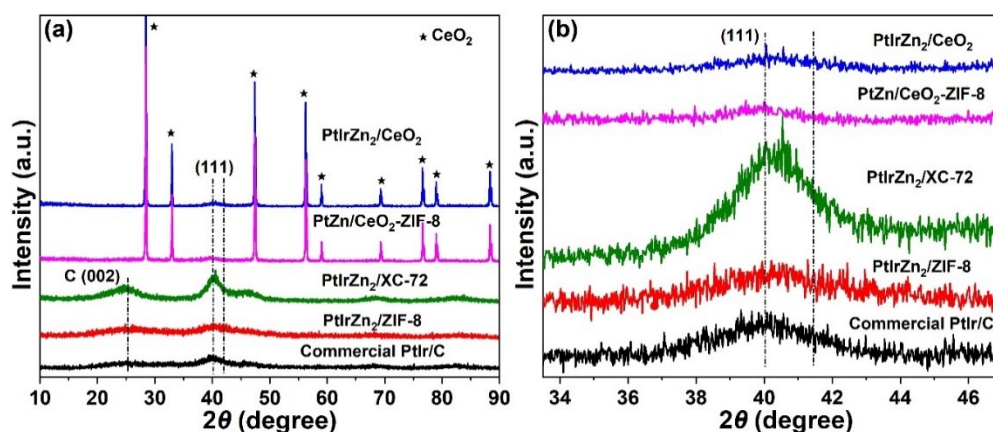
Figure S9. XRD patterns of the (a) commercial PtIr/C, PtZn/CeO$_2$-ZIF-8, PtIrZn$_2$/ZIF-8, PtIrZn$_2$/CeO$_2$, PtIrZn$_2$/XC-72, and PtIrZn$_2$/CeO$_2$-ZIF-8, and (b) the corresponding XRD patterns with enlarged region of 2θ from 33° to 47°. The XRD pattern results suggest the alloy state of these catalysts using Pt/ZIF-8 as the reference for pure Pt nanoparticles.

S12

Table S1. Elemental quantification (at.%) determined by XPS for different Pt-based catalysts.

Samples	C (at.%)	N (at.%)	O (at.%)	Ce (at.%)	Pt (at.%)	Ir (at.%)	Zn (at.%)
Commercial Pt/C	89.6		7.3		3.1		
Commercial PtIr/C	87.6		5.1		3.8	3.5	
PtIr/CeO$_2$-ZIF-8	66.9	6.9	11.8	4.8	2.0	2.3	5.3
PtIrZn$_2$/CeO$_2$-ZIF-8	54.9	7.5	14.8	3.4	9.2	7.3	2.9
PtIrZn$_2$/XC-72	97.1		1.9		0.1	0.2	0.7
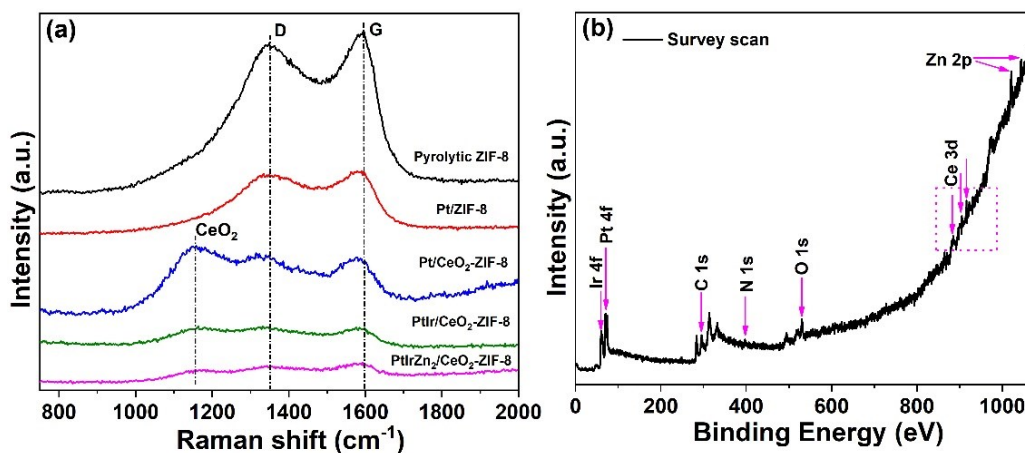
Figure S10. (a) Raman spectra of different catalysts. (1) The identical D band and G band of ZIF-8 derived carbon, as well as the CeO$_2$ peak, can be seen from the Raman spectra of these catalysts. (2) The pyrolytic ZIF-8 has a well-constructed carbon structure that is suitable for PGM nanoparticle deposition. (b) XPS survey scan of the PtIrZn$_2$/CeO$_2$-ZIF-8 confirms the presence of C, N, O, Ce, Pt, Ir, and Zn in the composite catalyst.
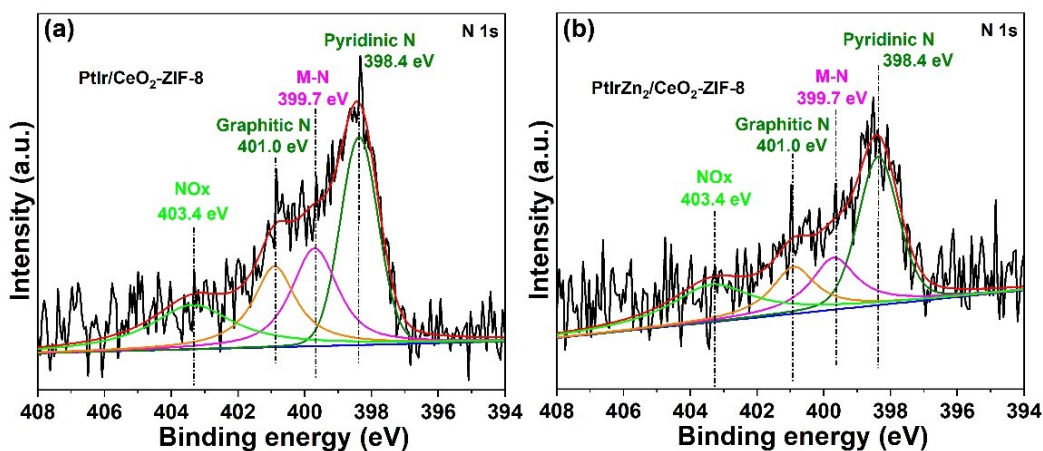
Figure S11. High-resolution XPS N 1s data for different catalysts: (a) PtIr/CeO$_2$-ZIF-8, and (b) PtIrZn$_2$/CeO$_2$-ZIF-8 indicates the presence of pyridinic-, graphitic-, and oxidized-N, as well as the M-N (M = Pt or Ir) in the ZIF-C.

Table S2. Binding energy comparison: high-resolution Pt 4f for some Pt-based catalysts, Δ_{B1} and Δ_{B2} represent binding energy differences between commercial Pt/C and other Pt alloy catalysts for Pt 4f$_{5/2}$ and Pt 4f$_{7/2}$, respectively.

Samples	Pt 4f$_{5/2}$ (eV)	Δ_{B1} (eV)	Pt 4f$_{7/2}$ (eV)	Δ_{B2} (eV)
Commercial Pt/C	75.34		72.10	
Commercial PtIr/C	75.10	−0.24	71.80	−0.30
PtIr/CeO$_2$-ZIF-8	74.74	−0.60	71.40	−0.70
PtIrZn$_2$/CeO$_2$-ZIF-8	74.70	−0.64	71.34	−0.76
PtIrZn$_2$/XC-72	74.92	−0.42	71.62	−0.48
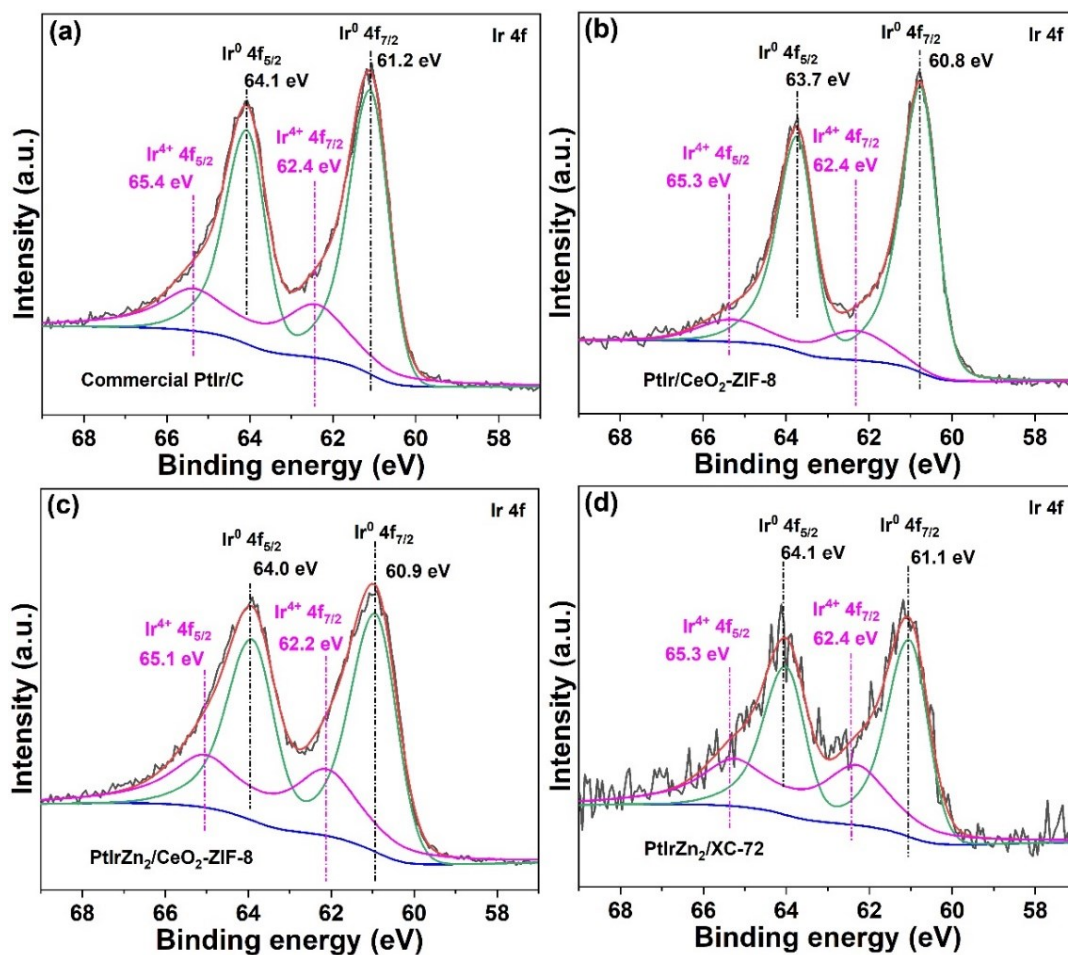
Figure S12. High-resolution XPS Ir 4f data for different catalysts: (a) commercial PtIr/C, (b) PtIr/CeO$_2$-ZIF-8, (c) PtIrZn$_2$/CeO$_2$-ZIF-8, and (d) PtIrZn$_2$/XC-72. These results indicate the possible shifts of binding energies for alloyed Ir in different catalysts.
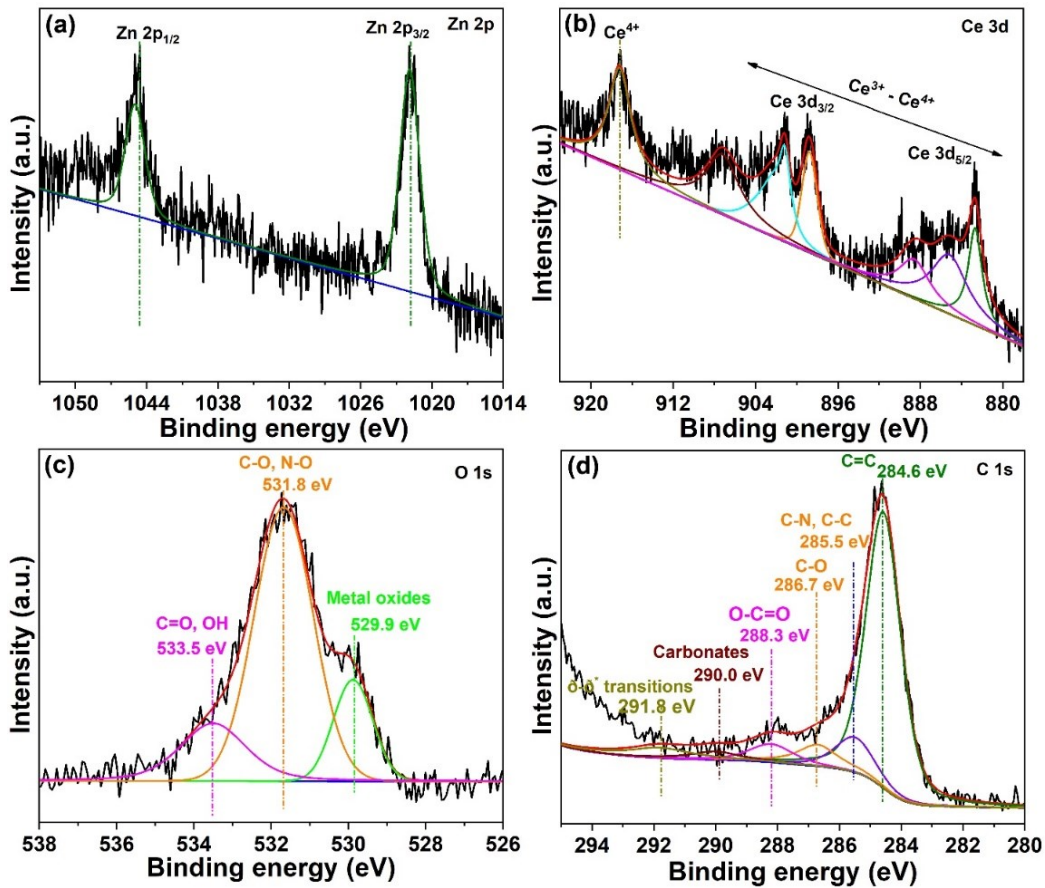
Figure S13. High-resolution XPS Zn 2p (a), Ce 3d (b), O 1s (c), and C 1s (d) of the PtIrZn$_2$/CeO$_2$-ZIF-8. These results indicate the possible energy shifts of banding energies for alloyed Zn, as well as binary support of CeO$_2$ and ZIF-C.
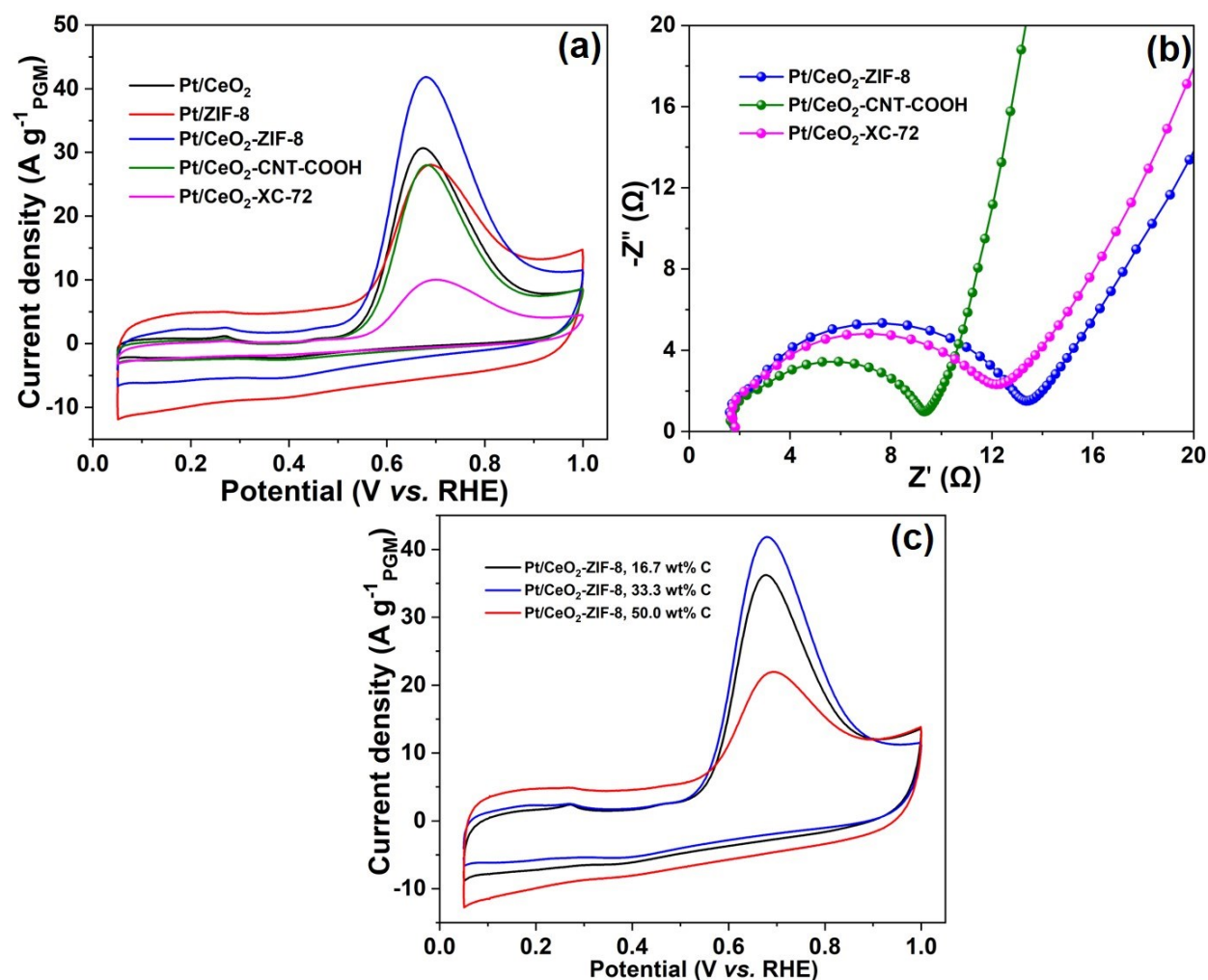
Figure S14. CV curves for different catalysts in Ar-saturated 1.0 M KOH + 0.1 M NH_3 at 5 mV s^{-1} and 900 rpm under ambient conditions: (a) Pt/CeO_2, $Pt/ZIF-8$, $Pt/CeO_2-ZIF-8$, $Pt/CeO_2-CNT-COOH$, and $Pt/CeO_2-XC-72$, and (c) comparison between Pt deposited on CeO_2 and ZIF-8 with different carbon contents. These comparisons suggest that $Pt/CeO_2-ZIF-8$ catalyst with 33.3wt% ZIF-8 carbon in the support leads to the highest AOR activity. (b) Nyquist plots of EIS spectra measured for $Pt/CeO_2-ZIF-8$, $Pt/CeO_2-CNT-COOH$, and $Pt/SiO_2-XC-72$ in 1.0 M KOH electrolyte at the open circuit potential. Based on the equivalent circuit model, the charge transfer resistance (R_{ct}) of these samples is estimated to be 8.8, 5.5, and 10.2 Ω, respectively, indicating small R_{ct} differences for them.
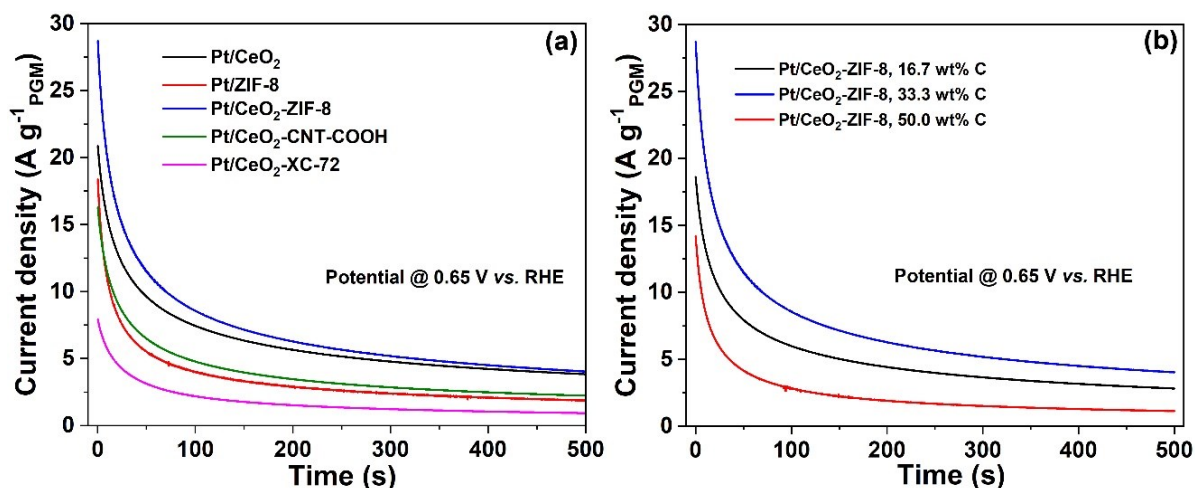
Figure S15. Chronoamperograms (CAs) of the different catalysts in Ar-saturated 1.0 M KOH + 0.1 M NH$_3$ at 900 rpm and 0.65 V *vs.* RHE under ambient conditions: (a) Comparison between commercial Pt/CeO$_2$, Pt/ZIF-8, Pt/CeO$_2$-ZIF-8, Pt/CeO$_2$-CNT-COOH, and Pt/CeO$_2$-XC-72, and (b) Comparison between Pt deposited on CeO$_2$-ZIF-8 with different ZIF-8 carbon contents. CA suggests the superiority of combination CeO$_2$ with ZIF-8 for Pt nanoparticle deposition for AOR.

Table S3. The AOR activity comparison of various catalysts.

Samples	Onset potential (V *vs.* RHE)	Current density (A g^{-1}) at 0.5 V *vs.* RHE	Peak current density (A g^{-1})
Pt/CeO$_2$-ZIF-8	0.504	2.9	41.8
PtIr/CeO$_2$-ZIF-8	0.417	6.3	15.7
PtZn/CeO$_2$-ZIF-8	0.468	3.7	19.9
Commercial PtIr/C	0.428	10.4	25.1
PtIrZn$_1$/CeO$_2$-ZIF-8	0.440	7.2	16.6
PtIrZn$_2$/CeO$_2$-ZIF-8	**0.345**	**15.7**	**31.8**
PtIrZn$_3$/CeO$_2$-ZIF-8	0.433	7.0	13.6
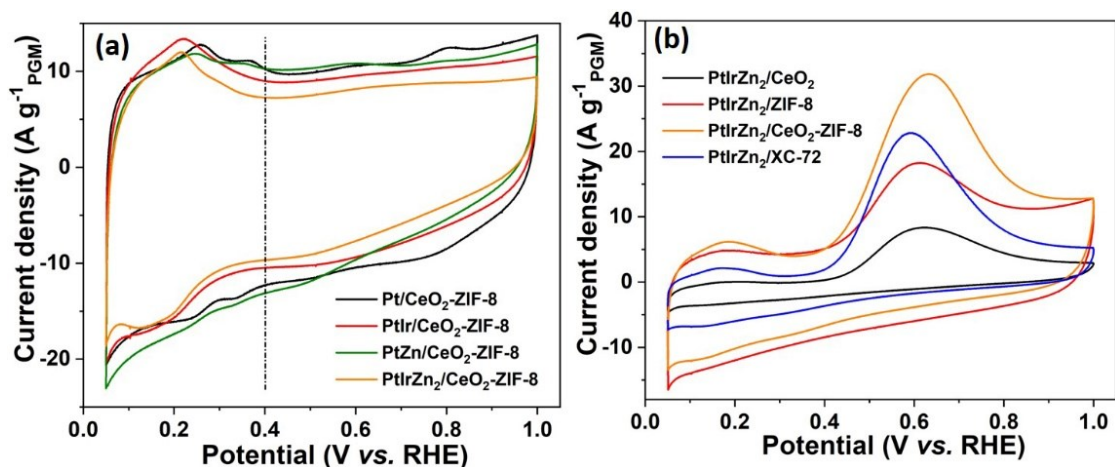
Figure S16. Baseline CV curves at 20 mV s^{-1} for Pt/CeO$_2$-ZIF-8, PtIr/CeO$_2$-ZIF-8, PtZn/CeO$_2$-ZIF-8, and PtIrZn$_2$/CeO$_2$-ZIF-8 catalysts in Ar-saturated 1.0 M KOH solutions. These results indicate that the currents associated with hydrogen adsorption-desorption are suppressed, compared to typical behaviors of Pt and PtIr catalysts without introducing Zn. (b) CV curves for different catalysts in Ar-saturated 1.0 M KOH + 0.1 M NH$_3$ at 5 mV s^{-1} and 900 rpm under ambient conditions: PtIrZn$_2$/CeO$_2$, PtIrZn$_2$/ZIF-8, PtIrZn$_2$/CeO$_2$-ZIF-8, and PtIrZn$_2$/ XC-72. This comparison suggests that CeO$_2$ and ZIF-8 carbon supports demonstrate a synergy for PtIrZn nanoparticles deposition, showing higher AOR activity than that of PtIrZn$_2$/XC-72.

Table S4. The estimated value of hydrogen adsorption-desorption area is based on **Figure S16**a.

Samples	The estimated value of hydrogen adsorption-desorption area
Pt/CeO$_2$-ZIF-8	0.430
PtIr/CeO$_2$-ZIF-8	0.694
PtZn/CeO$_2$-ZIF-8	0.192
PtIrZn$_2$/CeO$_2$-ZIF-8	0.629
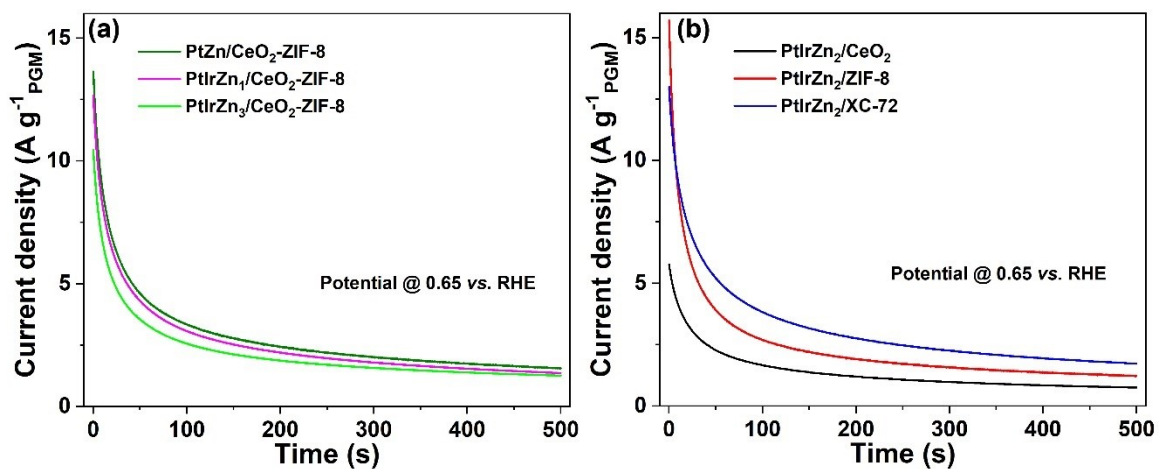
Figure S17. CAs of the different catalysts in Ar-saturated 1.0 M KOH + 0.1 M NH$_3$ at 900 rpm and 0.65 V *vs* RHE at room temperature: (a) Comparison between commercial PtZn/CeO$_2$-ZIF-8, PtIrZn$_1$/CeO$_2$-ZIF-8, and PtIrZn$_3$/CeO$_2$-ZIF-8, and (b) Comparison between Pt deposited on CeO$_2$, ZIF-8, and XC-72. The CA results from **Figure S17** and **Figure 5d** demonstrate the advanced support of CeO$_2$-ZIF-8 for effective PtIrZn nanoparticles deposition for the AOR.
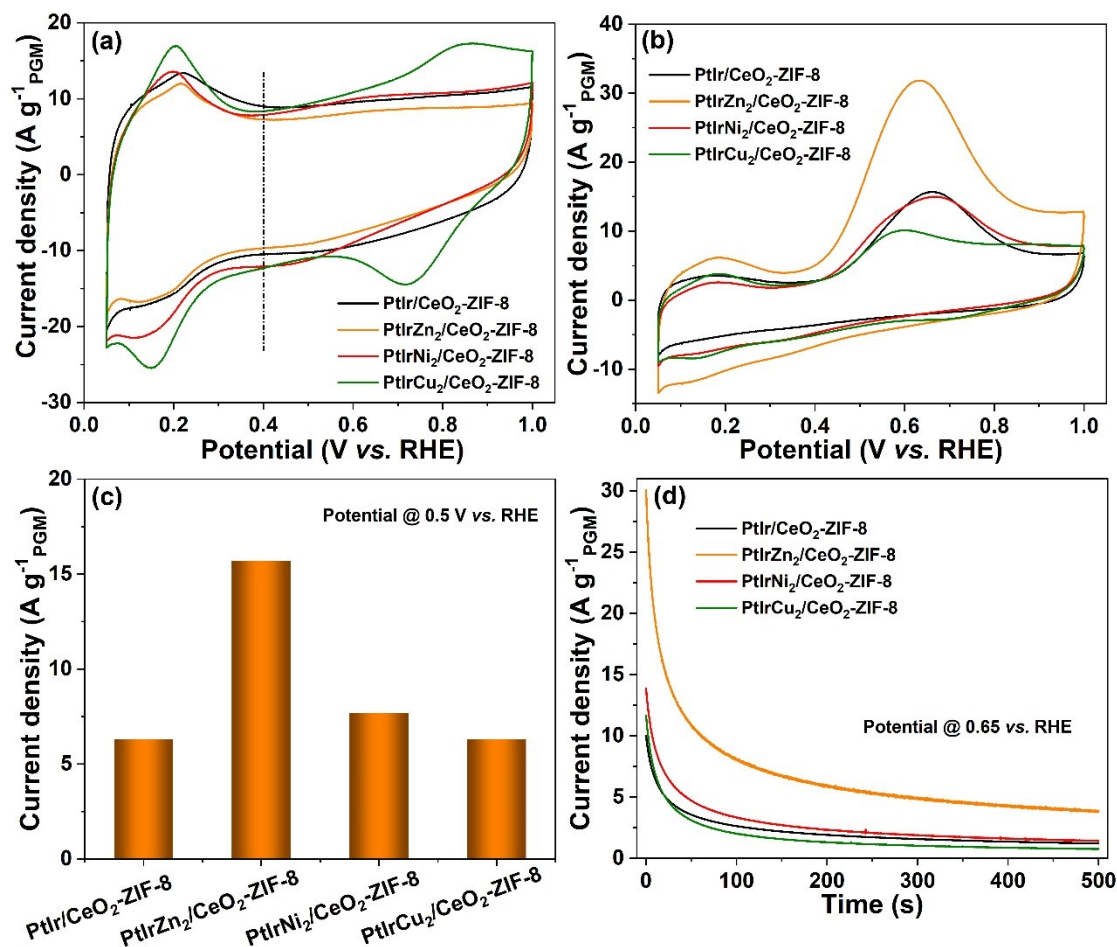
Figure S18. (a) Baseline CV curves at 20 mV s^{-1} for PtIr/CeO$_2$-ZIF-8, PtIrZn$_2$/CeO$_2$-ZIF-8, PtIrNi$_2$/CeO$_2$-ZIF-8, and PtIrCu$_2$/CeO$_2$-ZIF-8 catalysts in Ar-saturated 1.0 M KOH solutions. This indicates that the currents associated with hydrogen adsorption-desorption of PtIr alloys are suppressed with the addition of Zn, whereas the addition of Ni and Cu shows the opposite effect. (b) The corresponding CVs of these catalysts at 5 mV s^{-1} and 900 rpm in Ar-saturated 1.0 M KOH + 0.1 M NH$_3$ under room temperature. (c) Their AOR activity comparisons at 0.5 V *vs* RHE, and (d) CAs comparison at 0.65 V vs RHE. These results show that the addition of Zn could greatly enhance the intrinsic AOR activity of PtIr alloys, superior to that of the addition of Ni or Cu.

Table S5. AOR activity comparison of these different catalysts.

Samples	Onset potential (V $vs.$ RHE)	Current density (A g^{-1}) at 0.5 V $vs.$ RHE	Peak current density (A g^{-1})	References
PtIrZn$_2$/CeO$_2$	0.441	3.6	8.3	This work
PtIrZn$_2$/ZIF-8	0.395	10.9	18.2	This work
PtIrZn$_2$/CeO$_2$-ZIF-8	**0.345**	**15.7**	**31.8**	**This work**
PtIrZn$_2$/XC-72	0.424	12.4	22.8	This work
PtIrNi$_2$/CeO$_2$-ZIF-8	0.414	7.7	15.0	This work
PtIrCu$_2$/CeO$_2$-ZIF-8	0.418	6.3	10.1	This work
PtZn NCs/C	~0.50	–	405	[2]
PtIr/N-rGO (Pt:Ir = 1:3)	~0.37	–	–	[3]
PtIrNi$_1$/SiO$_2$-CNT-COOH (Pt:Ir = 9:1)	0.399	13.2	124.0	[4]
PtIrNi$_1$/CeO$_2$-CNT-COOH (Pt:Ir = 9:1)	0.465	5.4	34.0	[4]
CuPtRu (mass ratio Pt:Ru =7:1)	~0.49	10.0	180.0	[5]
Ir, Ni(OH)$_2$-Pt NCs/C (Pt:Ir = 8:2)	~0.51	–	–	[6]
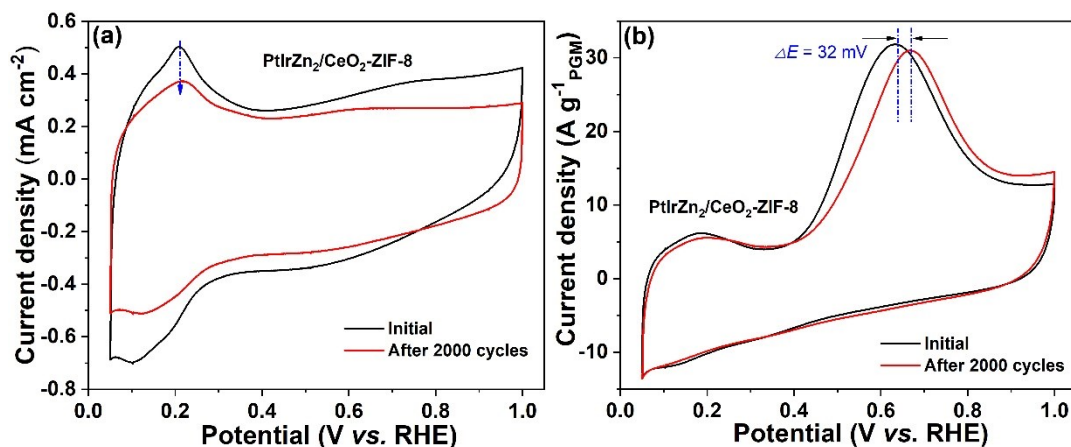
Figure S19. Catalyst stability tests for PtIrZn$_2$/CeO$_2$-ZIF-8 by cycling the potential of 0.05–0.7 V $vs.$ RHE in Ar-saturated 1.0 M KOH. (a) CVs before and after 2000 cycles were recorded in 1.0 M KOH at 20 mV s^{-1}, and (b) recorded in 1.0 M KOH + 0.1 M NH$_3$ at 5 mV s^{-1} and 900 rpm under room temperature. These results indicate that catalyst degradation occurs after CV cycling. The peak potential shows 32 mV positive shift, and peak current density shows a loss of ~3% after 2000 potential cycles.
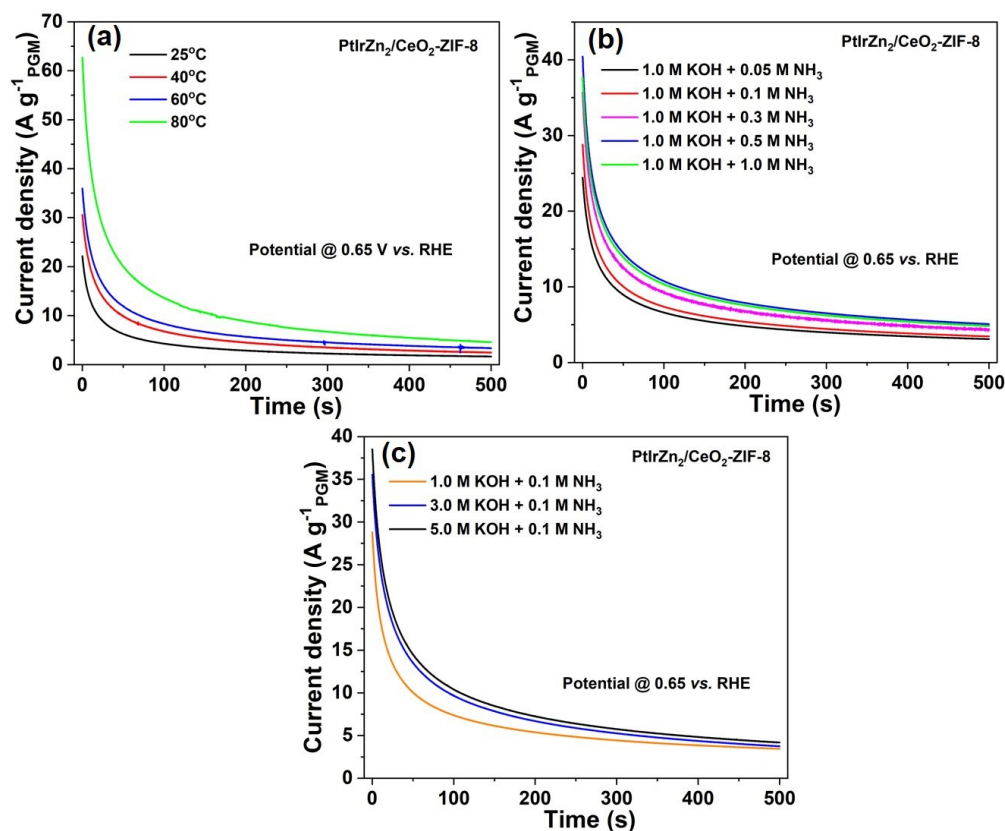
Figure S20. CAs of the PtIrZn$_2$/CeO$_2$-ZIF-8 catalyst at 900 rpm and 0.65 V *vs* RHE: (a) in Ar-saturated 1.0 M KOH + 0.1 M NH$_3$ at different operating temperatures, (b) in 1.0 M KOH in presence of different concentrations of NH$_3$ at room temperature, and (c) in different concentrations of KOH in presence of 0.1 M NH$_3$ at room temperature. These CA results are consistent with their corresponding CV characterization (**Figure 6**).
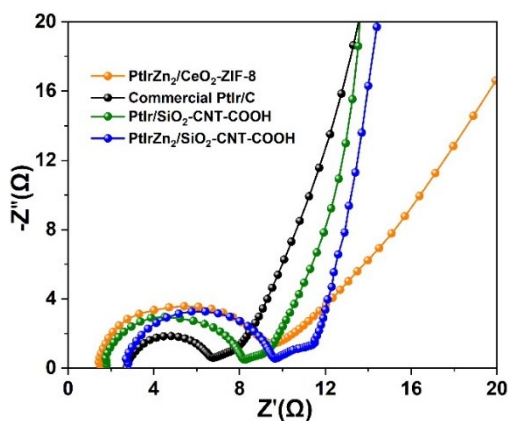
Figure S21. Nyquist plots of EIS spectra measured for PtIrZn$_2$/CeO$_2$-ZIF-8, commercial PtIr/C, PtIr/SiO$_2$-CNT-COOH, and PtIrZn$_2$/SiO$_2$-CNT-COOH in 1.0 M KOH electrolyte at the open circuit potential. The EIS results indicate the largest charge transfer resistance of the PtIrZn$_2$/CeO$_2$-ZIF-8 among all tested samples.

Table S6. Comparison of DAFC performance with literature results.

Electrolyte	Fuel	Anode catalyst	Cathode catalyst	Temperature (°C)	PPD (mW cm⁻²)	Reference
HEM (PAP-TP)	7 M NH_3 1.25 M KOH	$PtIrZn_2/CeO_2$-ZIF-8 1 mg_{PGM} cm^{-2}	Acta 4020 2 mg_{PGM} cm^{-2}	95	**91**	**This work**
HEM (PAP-TP)	7 M NH_3 1.25 M KOH	PtIr/C 1 mg_{PGM} cm^{-2}	Acta 4020 2 mg_{PGM} cm^{-2}	95	**241**	**This work**
HEM (PAP-TP)	7 M NH_3 1.25 M KOH	$PtIr/SiO_2$-CNT-COOH 1 mg_{PGM} cm^{-2}	Acta 4020 2 mg_{PGM} cm^{-2}	95	**282**	**This work**
HEM (PAP-TP)	7 M NH_3 1.25 M KOH	$PtIrZn_2/SiO_2$-CNT-COOH 1 mg_{PGM} cm^{-2}	Acta 4020 2 mg_{PGM} cm^{-2}	95	**314**	**This work**
KOH (54 wt% KOH)	NH_3 gas	$PtIr/B_4C$ 6.8 mg_{Pt} cm^{-2}	Pt 34 mg_{Pt} cm^{-2}	120	51	McKee et al.[7]
HEM (unspecified)	NH_3 (aq. Base)	2 mg_{PGM} cm^{-2}	PGM-free catalyst	100	450	Gottesfeld et al.[8]
HEM (PAP-TP)	3 M NH_3 1 M KOH	PtIr/C 2 mg_{PGM} cm^{-2}	Acta 4020 1 mg_{PGM} cm^{-2}	80	121	Zhao et al.[9]
HEM (PAP-TP)	3 M NH_3 3 M KOH	PtIr/C 2 mg_{PGM} cm^{-2}	Acta 4020 1 mg_{PGM} cm^{-2}	80	135	Zhao et al.[9]
PEM (Nafion 117)	5 M NH_3 1 M KOH	PdIr/C 2 mg_{PdIr} cm^{-2}	Pt/C 2 mg_{Pt} cm^{-2}	50	3.7	Assumpçao et al.[10]
PEM (Nafion 117)	3 M NH_3 3 M KOH	PtRh/C 2 mg_{PtRh} cm^{-2}	Pt/C 2 mg_{Pt} cm^{-2}	50	5.4	Assumpçao et al.[11]
PEM (Nafion 117)	5 M NH_3 1 M KOH	PtAu/C 1 mg_{Pt} cm^{-2}	Pt/C 1 mg_{Pt} cm^{-2}	40	2.6	Silva et al.[12]
HEM (Resin-PVA)	35 wt% NH_3	Cr-decorated Ni/C 10 mg cm^{-2}	MnO_2/C 20 mg_{MnO2} cm^{-2}	RT	11	Lan et al.[13]
HEM (AMI-7001)	NH_3 gas	Pt/C 0.45 mg_{Pt} cm^{-2}	Pt/C 0.45 mg_{Pt} cm^{-2}	RT	6.4	Siddiqui et al.[14]

References

1.   H. Zhang, S. Hwang, M. Wang, Z. Feng, S. Karakalos, L. Luo, Z. Qiao, X. Xie, C. Wang, D. Su, Y. Shao and G. Wu, *J. Am. Chem. Soc.*, 2017, **139**, 14143–14149.
2.   Y. T. Chan, K. Siddharth and M. Shao, *Nano Res.*, 2020, **13**, 1920–1927.
3.   Y. Zhou, G. Zhang, M. Yu, J. Xu, S. Qiao, X. Cheng and F. Yang, *ChemistrySelect*, 2018, **3**, 3433–3443.
4.   Y. Li, X. Li, H. Pillai, J. Lattimer, N. Mohd Adli, S. G. Karakalos, M. Chen, L. Guo, H. Xu, J. Yang, D. Su, H. Xin and G. Wu, *ACS Catal.*, 2020, **10**, 3945–3957.
5.   R. H. Manso, L. Song, Z. Liang, J. X. Wang and J. Chen, *ECS Trans.*, 2018, **85**, 177–182.
6.   K. Siddharth, Y. Hong, X. Qin, H. J. Lee, Y. T. Chan, S. Zhu, G. Chen, S.-I. Choi and M. Shao, *Appl. Catal., B*, 2020, **269**, 118821.
7.   D. W. McKee, J. A. J. Scarpellino, I. F. Danzig and M. S. Pak, *J. Electrochem. Soc.*, 1969, **116**, 562–568.
8.   S. Gottesfeld, *J. Electrochem. Soc.*, 2018, **165**, J3405–J3412.
9.   Y. Zhao, B. P. Setzler, J. Wang, J. Nash, T. Wang, B. Xu and Y. Yan, *Joule*, 2019, **3**, 2472−2484.
10. M. H. M. T. Assumpção, S. G. da Silva, R. F. B. De Souza, G. S. Buzzo, E. V. Spinacé, M. C. Santos, A. O. Neto and J. C. M. Silva, *J. Power Sources*, 2014, **268**, 129–136.
11. M. H. M. T. Assumpção, R. M. Piasentin, P. Hammer, R. F. B. De Souza, G. S. Buzzo, M. C. Santos, E. V. Spinacé, A. O. Neto and J. C. M. Silva, *Appl. Catal., B*, 2015, **174–175**, 136–144.
12. J. C. M. Silva, S. G. da Silva, R. F. B. De Souza, G. S. Buzzo, E. V. Spinacé, A. O. Neto and M. H. M. T. Assumpção, *Appl. Catal., A*, 2015, **490**, 133–138.
13. L. Rong and T. Shanwen, *Electrochem. Solid-State Lett.*, 2010, **13**, B83–B86.
14. O. Siddiqui and I. Dincer, *Fuel Cells*, 2018, **18**, 379–388.